Atmospheric Pressure and Velocity Fluctuations Near the Auroral Electrojet

J. G. Luhmann

Space Sciences Laboratory, Aerospace Corporation, El Segundo, California 90245

The low-frequency pressure and velocity perturbations caused by the temporally varying Lorentz force associated with auroral electrojet activity are modeled by calculating the disturbances generated by a two-dimensional, time-dependent current system in a gravitationally stratified, isothermal, windless atmosphere. These calculations provide information about the pattern of gravity waves around the hypothetical electrojet and give estimates of the magnitudes of near-field auroral disturbances in the middle atmosphere. It is suggested that the near-field vertical wind shears may be large enough to affect the development of air turbulence in the auroral zone.

INTRODUCTION

Dynamical perturbations of the auroral zone atmosphere by auroral activity have been observed at large distances from the auroral zone as low-frequency traveling ionospheric disturbances (TID's) [*Davis*, 1971] and locally as auroral infrasonic signals [*Wilson*, 1975]. Theoretical descriptions of the aforementioned effects have been considered by *Chimonas and Hines* [1970], *Chimonas* [1970], and *Chimonas and Peltier* [1970]. Additional analyses emphasizing various aspects of the atmosphere's dynamical response to auroral activity have been carried out by *Blumen and Hendl* [1969], *Testud* [1970], *Francis* [1974], *Chiu* [1976], and *Richmond and Matsushita* [1975]. Most of these authors have concentrated on the far-field disturbance with the exception of *Chimonas* [1970], who dealt with the infrasonic wave field near a pulsating aurora, and *Richmond and Matsushita* [1975], who were primarily concerned with modeling the global scale thermospheric (>80-km altitude) response to magnetic substorms. This paper describes a theoretical investigation of atmospheric dynamics in the immediate vicinity of a transient auroral electrojet. The method of analysis is similar to that used by *Chimonas and Hines* [1970] in a study related to the interpretation of mid-latitude TID's except that the far-field approximation is not invoked. The results, obtained by a combination of analytical and numerical methods, are used to estimate the magnitude of the pressure, velocity, and velocity shear perturbations in the atmosphere below the electrojet.

THEORY

Following *Chimonas and Hines* [1970], the atmosphere is treated as a compressible fluid upon which the electrojet acts as a perturbing force. Although both Joule heating and Lorentz forces contribute to the latter, it will be assumed, on the basis of several recent studies [*Hunsucker*, 1977; *Brekke*, 1979], that the Lorentz source is dominant. The atmosphere is assumed to be isothermal, windless, and nonviscous.

The standard fluid equations that are invoked for the present analysis are continuity

$$\frac{\partial \rho}{\partial t} + \nabla \cdot (\rho \mathbf{V}) = 0 \qquad (1)$$

momentum

$$\rho \frac{\partial \mathbf{V}}{\partial t} + \rho \mathbf{V} \cdot \nabla \mathbf{V} - \rho \mathbf{g} + \nabla p = \rho \mathbf{F} \qquad (2)$$

and heating (neglecting the Joule source)

$$\frac{\partial}{\partial t} (p\rho^{-\gamma}) + \mathbf{V} \cdot \nabla(p\rho^{-\gamma}) = 0 \qquad (3)$$

where ρ is the mass density, p is the pressure, $\mathbf{V}$ is the fluid velocity, g is the gravitational acceleration, and γ is the ratio of specific heats. The above notation has been chosen to conform to that used by *Chimonas and Hines* [1970]. The Lorentz force per unit mass, $\mathbf{F} = \mathbf{J} \times \mathbf{B}/\rho$, where $\mathbf{J}$ is the electrojet current and $\mathbf{B}$ is the magnetic field, is communicated by the moving ions to the neutral fluid by collisions. A rectangular coordinate system is chosen in which the z axis is vertical, x is in the north-south direction, and y is in the east-west direction.

Under the assumption that the unperturbed atmospheric density $\rho_0(z)$ and pressure $p_0(z)$ are proportional to $e^{-z/H}$, where H is the constant scale height, the fluid equations (1)–(3) can be linearized and Fourier-transformed in time to yield the set

$$i\omega\tilde{\rho} - \tilde{V}_z/H + \nabla \cdot \tilde{\mathbf{V}} = 0 \qquad (4)$$

$$i\omega\tilde{\mathbf{V}} + gH\nabla\tilde{p}_1 + (\tilde{p}_1 - \tilde{\rho}_1)\mathbf{g} = \mathbf{F} \qquad (5)$$

$$i\omega\tilde{p}_1 - \tilde{V}_z/H + \gamma\nabla \cdot \tilde{\mathbf{V}} = 0 \qquad (6)$$

where the tilde over the symbol denotes the transformed quantity

$$f(t) = \frac{1}{2\pi} \int_{-\infty}^{\infty} d\omega \, e^{i\omega t} f(\omega) \qquad (7)$$

and the subscripts 1 signify normalized perturbations of the form $(p - p_0)/p_0$.

Pressure Perturbation

Equations (4)–(6) combine to give an equation for p_1 analogous to (12) of Chimonas and Hines:

$$\nabla^2\tilde{p}_1 + \frac{\omega_g^2}{(\omega^2 - \omega_g^2)} \frac{\partial \tilde{p}_1}{\partial z^2} - \frac{\omega^2}{(\omega^2 - \omega_g^2)H} \frac{\partial \tilde{p}_1}{\partial z}$$

$$+ \frac{\omega^2}{(\omega^2 - \omega_g^2)4\omega_A^2 H^2} \tilde{p}_1 = \frac{1}{gH} \nabla \cdot \tilde{\mathbf{F}} \qquad (8)$$

where $\omega_A = \frac{1}{2}(\gamma g/H)^{1/2}$ is the acoustic cutoff frequency and $\omega_g = [(\gamma - 1)g/\gamma H]^{1/2}$ is the Brunt-Väisälä frequency. As was pointed out by these authors, the substitution

$$\tilde{p}_1 = e^{z/2H}\phi(x, z) \qquad (9)$$
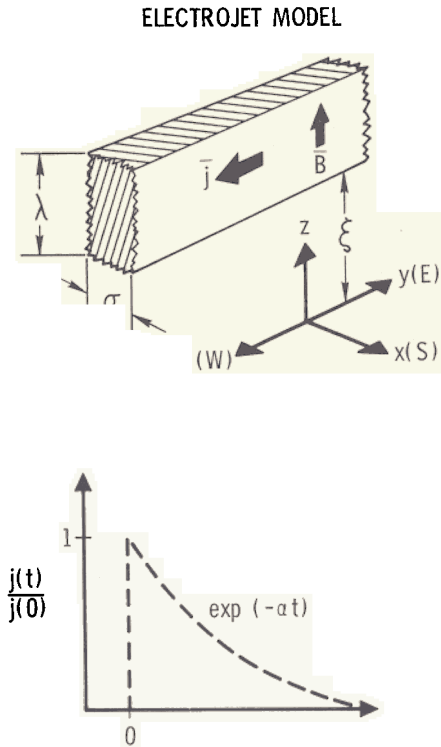
ELECTROJET MODEL

Fig.1.   Auroral electrojet model assumed in the calculation.

reduces (8) to the form

$$\frac{\partial \phi}{\partial x^2} + A_1 \frac{\partial \phi}{\partial z^2} + A_2 \phi = M_1 \qquad (10)$$

where

$$A_1 = \frac{\omega^2}{(\omega^2 - \omega^2)} \qquad (11)$$

$$\qquad (12)$$

$$C^2 = \gamma g H \qquad (13)$$

$$M_1 = e^{-z/2H}(\partial \tilde{F}_x/\partial x)/gH \qquad (14)$$

The procedure for solving (10) used here differs somewhat from that employed by Chimonas and Hines. First, it is assumed that the electrojet flows in the east-west direction and that it can be described by the current

$$\mathbf{J} = \hat{y}Af(z)g(x)T(t) \qquad (15)$$

In this case the Lorentz force for a vertical B field gives a form for M_1 given by

$$M_1 = Q\mathscr{I}(z)G(x)\tilde{T}(\omega) \qquad (16)$$

where

$$Q = BA/gH \qquad (17)$$

$$\mathscr{I}(z) = e^{-z/2H}[f(z)/\rho(z)] \qquad (18)$$

$$G(x) = dg(x)/dx \qquad (19)$$

Two successive Fourier transformations of (10) in the spatial variables x and z then lead to the equation

$$(-k_x^2 - A_1 k_z^2 + A_2)\widetilde{\widetilde{\phi}} = Q\tilde{\mathscr{I}}(k_z)\tilde{G}(k_x)\tilde{T}(\omega)$$

Equation (20) can be solved for an infinite atmosphere if the functions used in the description of the electrojet current are carefully chosen. The model selected for the present analysis is shown in Figure 1. If a box function is selected to represent the sharp north-south boundary of an auroral electrojet,

$$g(x) = 0 \qquad\qquad x < \eta$$

$$g(x) = 1 \qquad\qquad \eta < x < \eta + \sigma$$

$$g(x) = 0 \qquad\qquad x > \sigma + \eta$$

then

$$G(x) = dg(x)/dx = \delta(x - \eta) - \delta(x - \eta - \sigma) \qquad (22)$$

and the x dependence of the right-hand side of (20) is contained in the transformed function

$$\tilde{G}(k_x) = -i(e^{ik x^\eta} - e^{ik x^{(\eta+\sigma)}})/k_x \qquad (23)$$

It follows that the Fourier inversion in x gives

$$\tilde{\phi} = Q\tilde{\mathscr{I}}(k_z)\tilde{T}(\omega)(1/\omega_0)[\sin \omega_0(x - \eta) - \sin \omega_0(x - \eta - \sigma)]$$

$$\qquad (24)$$

where

$$\omega_0 = [-A_1 k_z^2 + A_2]^{1/2}$$

If the altitude dependence of M_1 is approximated by

$$\mathscr{I}(z) = e^{-z/2H}f(z)/\rho(z) \approx 0 \qquad\qquad z < \xi$$

$$\mathscr{I}(z) = e^{-z/2H}f(z)/\rho(z) \approx 1/\rho_0(0) \qquad \xi < z < \xi + \lambda$$

$$\mathscr{I}(z) = e^{-z/2H}f(z)/\rho(z) \approx 0 \qquad\qquad z > \xi + \lambda$$

the inversion in z, performed with the aid of the convolution theorem [e.g., Butkov, 1968], gives

$$\phi = \frac{-Q\tilde{T}(w)}{\rho_0(0)} \frac{1}{(-A_1)^{1/2}} \int_\xi^{\xi+\lambda} ds[J_0(X_1) - J_0(X_2)] \qquad (27)$$

in which the arguments of the zero-order Bessel functions J_0 are

$$X_1 = (-A_2/A_1)^{1/2}[-A_1(x - \eta)^2 - (z - s)^2]^{1/2} \qquad (28)$$

$$X_2 = (-A_2/A_1)^{1/2}[-A_1(x - \eta - \sigma)^2 - (z - s)^2]^{1/2} \qquad (29)$$

A final inverse transformation is needed to obtain the fractional pressure pulse from ϕ:

$$P_1(x, z, t) = \frac{1}{(2\pi)^{1/2}} \int_{-\infty}^\infty \tilde{p}_1 e^{i\omega t} d\omega = \frac{e^{z/2H}}{(2\pi)^{1/2}} \int_{-\infty}^\infty \phi e^{i\omega t} d\omega$$

$$\qquad (30)$$

The inverse transform of the Bessel function in the integrand of (27) can be found in tables for the low-frequency ($\omega \ll \omega_g$) limit, since the approximations

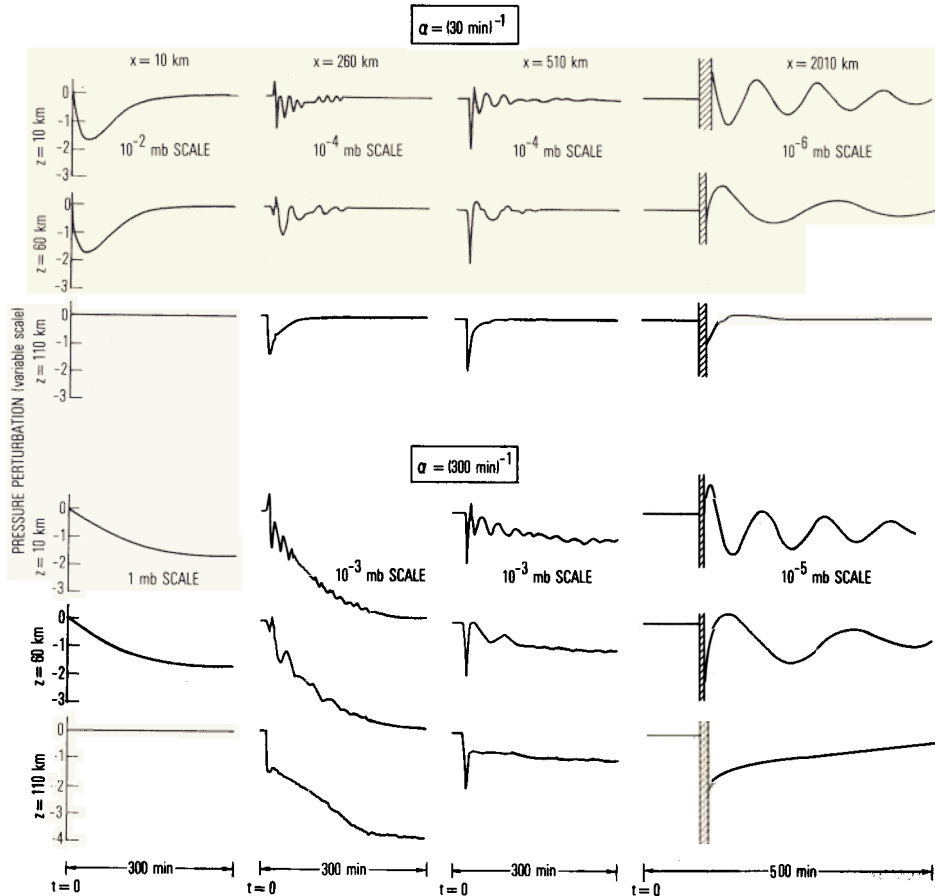$$A_1 \approx -\omega^2/\omega_g^2 \qquad A_2 \approx -A_1\omega_A^2/C^2 \qquad (31)$$

Fig. 2. Time histories of the pressure perturbation at various altitudes and ranges from the electrojet described in the text. The scale for the $x = 2010$ km results is magnified to show the details of the oscillations that follow the initial transient. Off-scale values are indicated by cross-hatching.

can be made. The arguments ((28) and (29)) then take the form $b(\omega^2 - a^2)^{1/2}$, in which case the inverse is

$$\int_{-\infty}^{\infty} d\omega \; e^{i\omega t} J_0[b(\omega^2 - a^2)^{1/2}] = 0 \qquad t < b$$

$$\int_{-\infty}^{\infty} d\omega \; e^{i\omega t} J_0[b(\omega^2 - a^2)^{1/2}] = \frac{4i \cos\,[a(t^2 - b^2)^{1/2}]}{(t^2 - b^2)^{1/2}} \qquad t > b$$

$$(32)$$

If the inverse transform of $\bar{T}(\omega)/\omega$ can be found, the convolution theorem can be used once again to evaluate the low-frequency response for (30). The function $T(t) = e^{-\alpha t}S(t)$, shown in Figure 1, bears a reasonable resemblance to the temporal behavior of an auroral storm and gives an imaginary transform for $\bar{T}(\omega)/\omega$ of the form

$$\text{Im} \int_{-\infty}^{\infty} d\omega \; e^{i\omega t} \frac{\bar{T}(\omega)}{\omega} = \frac{2\pi}{\alpha} e^{-\alpha t} \qquad (33)$$

The convolution theorem subsequently leads to

$$P_1(x, z, t) = \frac{Q\omega_g e^{z/2H}}{\rho_0(0)\alpha} \left\{ \int_{b_1}^{t} d\tau \int_{\xi}^{\xi+\lambda} ds \; e^{-\alpha(t-\tau)} \right.$$

$$\cdot \left[\cos \left[\frac{\omega_g(z-s)}{(x-\eta)} \left(\tau^2 - \left(\frac{\omega_A}{C\omega_g}(x-\eta) \right)^2 \right)^{1/2} \right] \middle/ \left(\tau^2 - \left(\frac{\omega_A}{C\omega_g}(x-\eta) \right)^2 \right)^{1/2} \right]$$

$$- \int_{b_2}^{t} d\tau \int_{\xi}^{\xi+\lambda} ds \; e^{-\alpha(t-\tau)} \left[\cos \left[\frac{\omega_g(z-s)}{(x-\eta-\sigma)} \left(\tau^2 \right. \right. \right.$$

$$- \left(\frac{\omega_A}{C\omega_g}(x-\eta-\sigma) \right)^2 \right)^{1/2} \right] \middle/ \left(\tau^2 - \left(\frac{\omega_A}{C\omega_g}(x-\eta-\sigma) \right)^2 \right)^{1/2} \right\} \quad (34)$$

for

$$b_1 = |(\omega_A/C\omega_g)(x-\eta)| \qquad (35)$$

$$b_2 = |(\omega_A/C\omega_g)(x-\eta-\sigma)| \qquad (36)$$

The integration over s can be done analytically:

$$p_1(x, z, t) = \frac{Q\omega_g e^{z/2H}}{\rho_0(0)\alpha} \int_{b_1}^{t} d\tau \; e^{-\alpha(t-\tau)}$$

$$\left[[\sin B_1(\xi + \lambda - z) - \sin B_1(\xi - z)] \middle/ \left(B_1^2 \frac{(x-\eta)}{\omega_g} \right) \right]$$

$$- \int_{b_1}^{t} d\tau \; e^{-\alpha(t-\tau)} \left[[\sin B_2(\xi + \lambda - z) \right.$$

$$\left. - \sin B_2(\xi - z)] \middle/ \left(B_2^2 \frac{(x-\eta-\sigma)}{\omega_g} \right) \right] \qquad (37)$$

Here B_1 and B_2 are given by

$$B_1 = \left[\tau^2 - \left(\frac{\omega_A}{C\omega_g}(x-\eta) \right)^2 \right]^{1/2} \frac{\omega_g}{(x-\eta)} \qquad (38)$$

$$B_2 = \left[\tau^2 - \left(\frac{\omega_A}{C\omega_g}(x-\eta-\sigma) \right)^2 \right]^{1/2} \frac{\omega_g}{(x-\eta-\sigma)} \qquad (39)$$
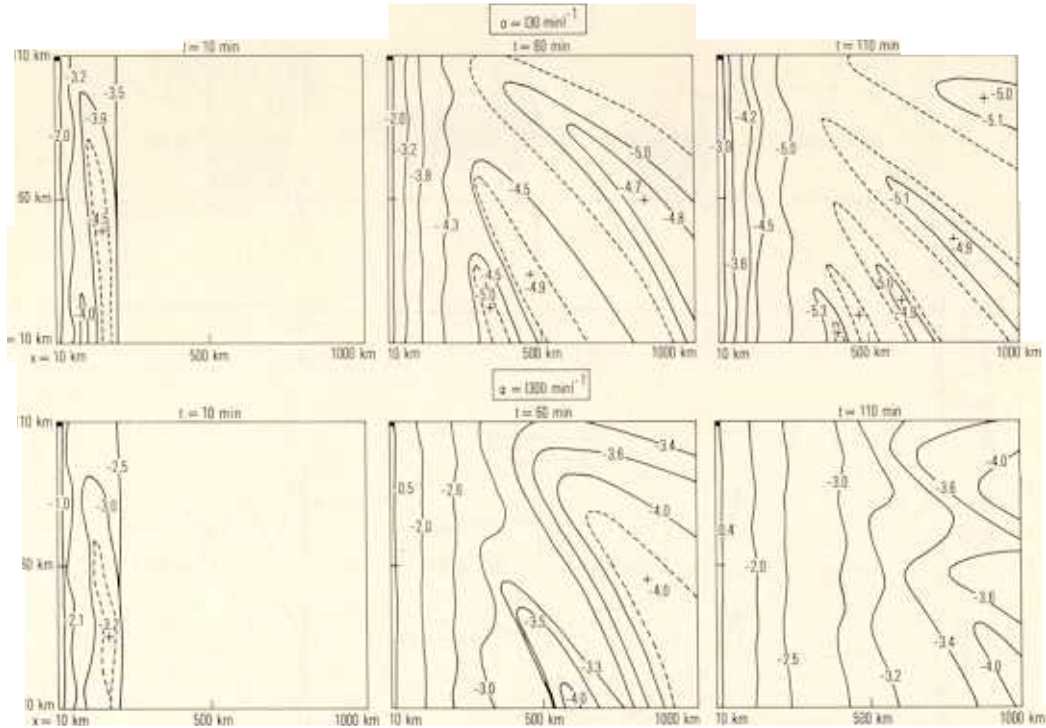
Fig. 3. Calculated patterns of the pressure perturbation around the model electrojet at three different times. The electrojet is located in the upper left corner. Contour labels indicate the logarithm of the pressure perturbation magnitude in millibars. The dashed contours show the location where the sign of the perturbation goes through zero. Pluses identify regions of positive perturbation; the regions on the outside of the dashed contours have negative perturbations or subquiescent pressure. The patterns are symmetric about $z = \xi + \lambda/2$ and change sign at the electrojet midplane $x = \eta + \sigma/2$.

The remaining integration over τ must be carried out numerically.

Velocity Perturbation

Because the ω transform of the horizontal velocity perturbation u is related to the transform of the pressure perturbation by the momentum equation (5),

$$\bar{u}(x, z, \omega) = -\frac{1}{i\omega}\left[Hg\frac{\partial \bar{p}_1}{\partial x} - \tilde{F}_x\right] \quad (40)$$
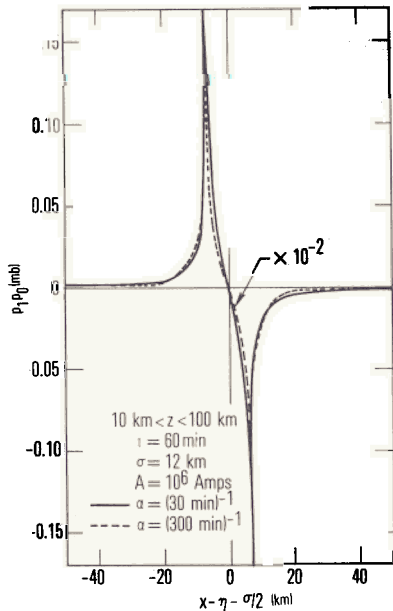

Fig. 4. Calculated near-field pressure perturbation at $t = 60$ min.

a differential equation for u analogous to (10) can be written

$$\frac{\partial^2 \Xi}{\partial x^2} + A_1\frac{\partial^2 \Xi}{\partial z^2} + A_2\Xi = M_2 \quad (41)$$

where

$$\Xi = e^{-z/2H}\tilde{u}$$

$$M_2 = -\frac{Hg}{i\omega}\frac{\partial M_1}{\partial x}$$

for the domain outside the range $\eta < x < \eta + \sigma$ directly beneath the electrojet. Proceeding as in the calculation of the pressure perturbation, a solution is obtained by the use of Fourier transforms;

$$u(x, z, t) = \frac{Q'\omega_g e^{z/2H}}{\rho_0(0)\alpha^2}\left\{\int_{b_1}^{t}d\tau\,[(e^{-\alpha(t-\tau)}\right.$$

$$- 2\alpha(t-\tau))\,(\cos B_1\,(\xi + \lambda - z)$$

$$- \cos B_1\,(\xi - z))/(B_1(x - \eta)/\omega_g)]$$

$$- \int_{b_2}^{t}d\tau\,[(e^{\alpha(t-\tau)} - 2\alpha\,(t-\tau))(\cos B_2\,(\xi + \lambda - z)$$

$$\left. - \cos B_2(\xi - z)/(B_2\,(x - \eta - \sigma)/\omega_g)]\right\} \quad (44)$$
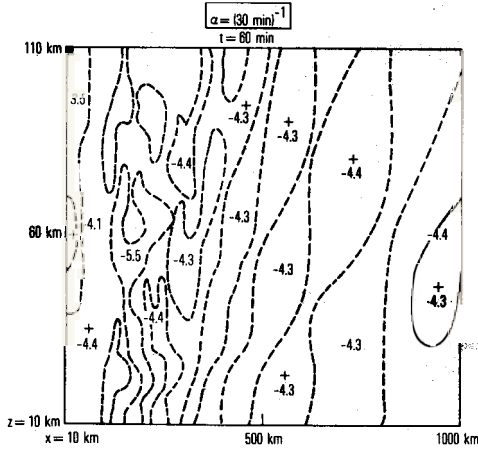
where

$$Q' = QC^2/\gamma$$

Fig. 5. Calculated pressure pattern with the earth-reflected component added for the case $\alpha = (30 \text{ min})^{-1}$, $t = 60$ min. The format of this contour diagram is described in the legend of Figure 2.

The corresponding vertical shear of the horizontal wind is also of interest:

$$\frac{\partial u}{\partial z}(x, z, t) = -\frac{u(x, z, t)}{2H} - \frac{Q'\omega_g e^{z/2H}}{\rho_0(0)\alpha^2}$$

$$\cdot \left\{ \int_{b_1}^{t} d\tau[(e^{-\alpha(t-\tau)} - 2\alpha(t-\tau))(\sin B_1(\xi + \lambda - z)) \right.$$

$$- \sin B_1(\xi - z))/((x-\eta)/\omega_g)]$$

$$+ \int_{b_2}^{t} d\tau[(e^{-\alpha(t-\tau)} - 2\alpha(t-\tau))(\sin B_2(\xi + \lambda - z))$$

$$\left. - \sin B_2(\xi - z))/((x-\eta-\sigma)/\omega_g)] \right\} \quad (46)$$

COMPUTATIONAL RESULTS AND DISCUSSION

Figure 2 shows some time histories of the pressure perturbation at various ranges and altitudes below the electrojet calculated from (37) with the representative values $A\sigma\lambda = 10^6$ A, $\sigma = 12$ km, $\eta = 0$ km, $\xi = 100$ km, $\lambda = 20$ km, $H = 10^4$ m, $g = 9.5$ m s^{-2}, $\gamma = 1.4$, $\omega_A = \frac{1}{2}(\gamma g/H)^{1/2}$, $\omega_g = 0.017$ s^{-1}, $B = 6 \times 10^{-5}$ W m^{-2}, and $\rho_0(0) = 1.23$ kg m^{-3}, for $\alpha = (30 \text{ min})^{-1}$ and $\alpha = (300 \text{ min})^{-1}$. Although the actual temporal behavior and spatial morphology of the electrojet are not well known [Francis, 1974], these parameters, together with the model shown in Figure 1, approximate some of the characteristics deduced from radar observations [Greenwald et al., 1973, 1975; Brekke and Rino, 1978]. Since the mathematical treatment was carried out for the limit of low frequencies, temporal structures with time scales of >10 min are presumably valid results. The fast transients seen in Figure 2 are questionable features which may be related in part to high-frequency components in the electrojet time structure, especially at onset (see Figure 1). Caution must also be exercised in the application of the quasi-linear calculation at altitudes where the magnitude of the perturbation becomes comparable to the ambient pressure. Because the solution is symmetric about $z = \xi + \lambda/2$, the oscillations at $z = 10$ km can be compared with the characteristics of TID's which are observed at an altitude of 200 km, where the pressure is $\sim 10^{-6}$ mbar. *Chimonas and Hines* [1970] imply that typical $\sim$1-hr period perturbations of a few percent are seen 3000 km equatorward of the auroral zone, consistent with the results shown in Figure 2.

Another view of the spatial and temporal development of the pressure perturbation is seen in Figure 3, which shows how the sinusoidal oscillations, which belong to the class of gravity waves, develop at distances from the source where significant dispersion of the Fourier components occurs. This figure also illustrates the direction of phase propagation, which is normal to the direction of energy propagation from the source as expected for gravity waves [*Beer*, 1974]. These patterns are symmetric about $z = \xi + \lambda/2$ and change sign at the source midplane $x = \eta + \sigma/2$ where the Lorentz force switches direction between toward and away from the electrojet.

An amplified view of the very near field of the pressure perturbation is given in Figure 4. Here the maximum disturbance, which becomes infinite at the site of the N-S boundaries of the model electrojet ($x - \eta = 0$ and $x - \eta = \sigma$), is seen. Because the sharp vertical-edge geometry of the model is unrealistic, this behavior is an artifact; however, the nearby perturbations of $\lesssim 0.1$–1.0 mbar may be realized in nature if the electrojet edge is fairly localized in range. Of course, a perturbation of this magnitude is too large to be considered linearly at altitudes of $\gtrsim 50$ km.

The earth-reflected wave discussed by *Francis* [1974] can be easily included if it is assumed to be reflected with efficiency ϵ and is describable by an image source at $z = -(\xi + \lambda/2)$:

$$p_{1 \text{ total}} = p_1(x, z, t, \xi, \lambda) + \epsilon p_1(x, z, t, -\xi, -\lambda)$$

An example of the modification of the pressure pattern with the total ($\epsilon = 1$) reflected component added is shown in Figure
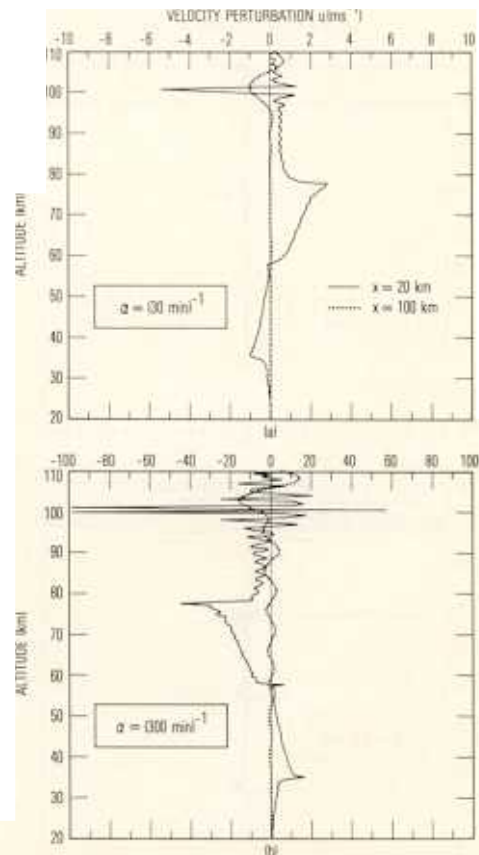

Fig. 6. Altitude profiles of the horizontal wind velocity perturbation by the model electrojet at the ranges $x = 20$ km and $x = 100$ km calculated from (44) for $t = 60$ min: (a) $\alpha = (30 \text{ min})^{-1}$; (b) $\alpha = (300 \text{ min})^{-1}$. The altitude resolution is 0.5 km. The structure at $\sim$20-km altitude intervals results from the altitude structure of the source.
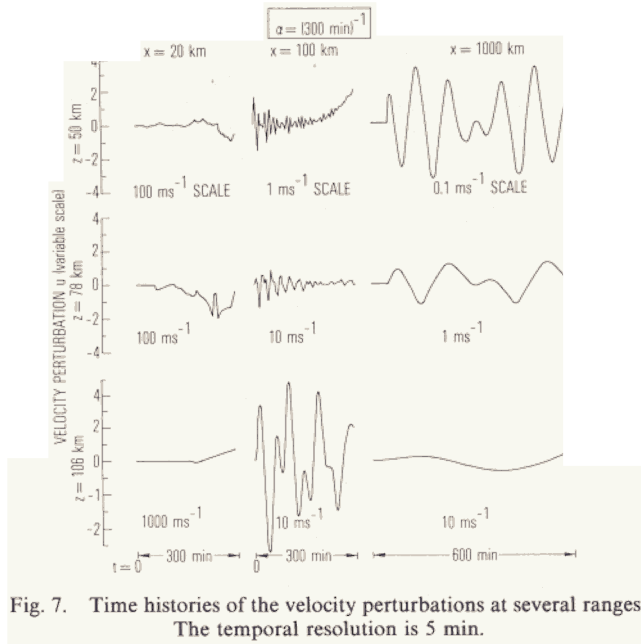
Fig. 7. Time histories of the velocity perturbations at several ranges. The temporal resolution is 5 min.
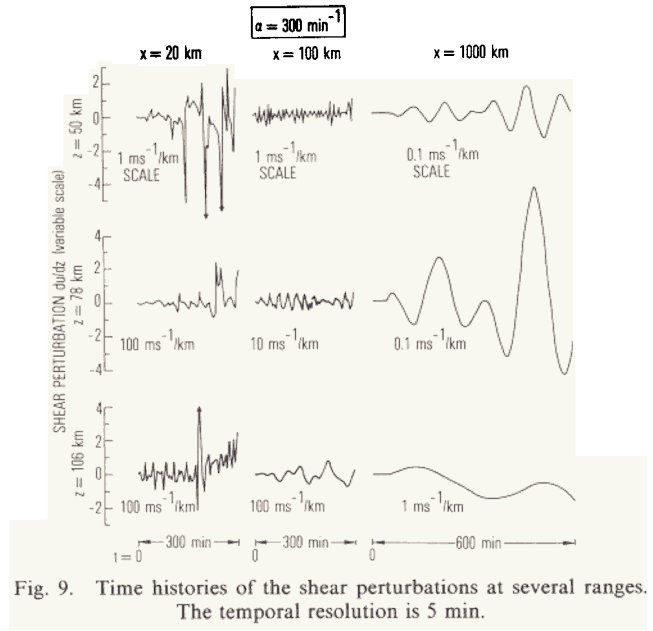

Fig. 9. Time histories of the shear perturbations at several ranges. The temporal resolution is 5 min.

5. It can be seen from Figure 5 that the pressure pattern becomes more complicated but, more important, that the very near field magnitude is evidently reduced substantially by destructive interference with the direct perturbation. Since the reflection properties of the boundary layer are probably variable, Figures 3 and 5 represent extreme cases.
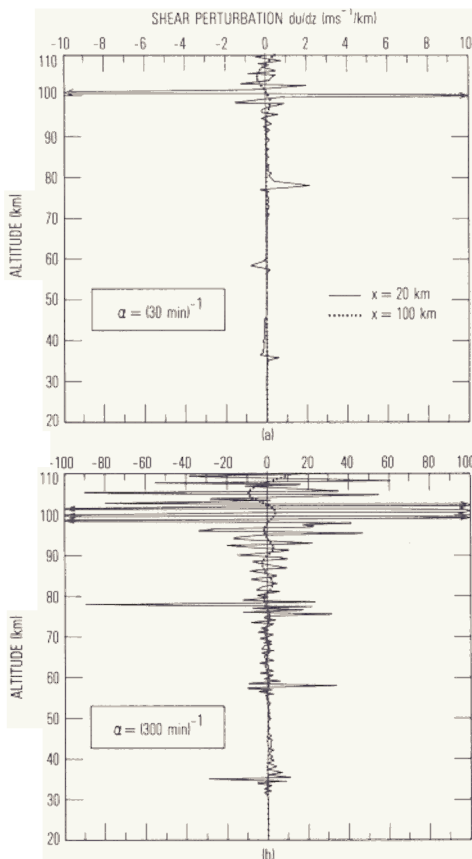

Fig. 8. Altitude profiles of the horizontal wind shear corresponding to the cases shown in Figure 6 as calculated from (46): (a) $\alpha = (30 \text{ min})^{-1}$; (b) $\alpha = (300 \text{ min})^{-1}$. The spatial resolution is 0.5 km.

The velocity perturbation described by (44) is quite structured in comparison to the pressure perturbation and so is not easily displayed as a contour diagram. Figure 6 shows some representative altitude profiles of the velocity perturbation at two different ranges. Examples of the time histories of these perturbations for the case $\alpha = (300 \text{ min})^{-1}$ are given in Figure 7. As was noted in the discussion of the pressure perturbations that were shown in Figure 2, rapid time scale ($\lesssim 10$ min) fluctuations, which appear to dominate the velocity spectrum at $x = 20$ km where very large perturbations are seen, are of questionable validity. However, low-frequency ($\omega < \omega_g$) variations of ~ 20–30 m s^{-1} are clearly present in some of the wave forms, especially at $x = 100$ km. A more precise determination of the low-frequency content of these results could in principle be obtained by a numerical Fourier analysis, but this additional computation has not been carried out at the present time. The corresponding vertical shears of the velocity can be inferred from Figure 6 or calculated from (46). The latter method produced the altitude profiles and time histories displayed in Figures 8 and 9, respectively. Even if the high-frequency component is disregarded, it is apparent that shears of up to ~ 10 m s^{-1} km^{-1} occur when the value $\alpha = (300 \text{ min})^{-1}$ is used. Not surprisingly, the long-lived auroral activity produces the stronger low-frequency effects.

At this point in the discussion it is useful to point out that all of the above results can be rather easily extended to other electrojet current strengths and scale sizes. The former modification involves straightforward renormalization. Structured or latitudinally wider electrojet geometries produce perturbations that can be constructed from superpositions of the given patterns, appropriately shifted in latitude in accordance with the source distribution.

Among the results, velocity shears are of particular interest because they have been found to influence the potential for air turbulence at a specific location. In particular, a standard index which is used as a measure of instability is the gradient Richardson number [Woods, 1969]

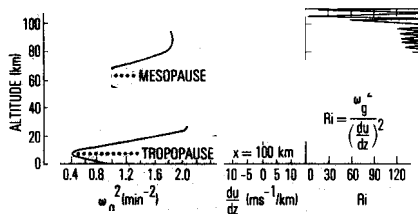$$Ri = \frac{\omega_g^2}{(\partial u / \partial z)^2} \qquad (47)$$

Fig. 10. (a) Approximate altitude dependence of the square of the Brunt-Väisälä frequency. (b) The velocity shear perturbation of Figure 8b. (c) The value of Ri calculated from these quantities.

Turbulence in both the ocean and the atmosphere is found to be correlated with large vertical shears in velocity and with small Richardson numbers, but the definition of the threshold or critical values appears to vary with the circumstances. For example, Waco [1970] found empirically that stratospheric clear air turbulence (CAT) was likely to occur in regions where the wind shear exceeded ~2.5 m s^{-1} km^{-1} and where Ri was less than 15. Unfortunately, a similar analysis for the upper middle atmosphere does not appear to have been carried out. Nevertheless, it is interesting to note that wind shears with a low-frequency component of the order of the aforementioned magnitude are found for the case of the slowly decaying electrojet event if the current is reduced from 10^6 to 10^5 A. If one conservatively adopts the velocity shear profile at $x = 100$ km from Figure 8b, for which the low-frequency content is clearly distinguishable in Figure 9, Richardson numbers for a particular time and location in the perturbed zone can be estimated. The average magnitude of the Brunt-Väisälä frequency in the low and middle atmosphere is shown in Figure 10a. As is seen here, the actual value of ω_g is not constant, as was assumed in the calculations, but varies with altitude because of the temperature structure of the atmosphere according to

$$\omega_g^2 = -g\left(\frac{1}{\rho}\frac{\partial\rho}{\partial z} - \frac{g}{\gamma RT}\right) \quad (48)$$

where R is the gas constant. If it is assumed that the auroral activity affects the wind shear more than it affects ω_g, the Richardson number in the vertical cross section corresponding to the shear perturbation of Figures 8b and 10b is given by Figure 10c. Layers of small Richardson number occur near the altitude of the electrojet, suggesting the possibility of upper mesophere turbulence generation by auroral activity. Although the effects discussed above are restricted to high altitudes, it is worthwhile to note that the local minima in ω_g at the mesopause and tropopause make these regions particularly susceptible to turbulence because Ri for a particular wind shear is automatically smaller there. The addition of an ambient wind shear to the wave-induced shear could further increase the probability of CAT or, alternatively, suppress instability depending on whether the auroral perturbations enhance or reduce the local background shear. Of course, these inferences are based on a calculation with many potential sources of error; moreover, ω_g is probably affected by both background and aurorally induced temperature and density variations.

QUALIFICATIONS AND CONCLUDING REMARKS

A major point of concern in the above calculations is the assumption of an isothermal atmosphere. However, Francis [1974] has argued that no strong ducting mechanisms operate for the waves considered in both his own report and here. Free propagation below 100-km altitude, with the exception of the boundary at the surface of the earth, was also assumed in that author's earlier analysis of medium scale TID's. The full nonisothermal calculation must be carried out by methods [e.g., Friedman, 1966] which are outside the scope of this work. The effects of ambient winds [e.g., Hines and Reddy, 1967] are also not incorporated in the present effort for similar reasons. Moreover, the application of linear perturbation theory here can be questioned, as was discussed above, as can the credibility of the high-frequency component of the calculated results. The magnitude and geometry of the assumed electrojet model may also be challenged. The sharp edges of the volume containing the current can produce unrealistic features in the solution; furthermore, substorms are often found to have electrojet currents of only 10^5 A and meridional extents of several hundred kilometers. Thus the calculated effects are likely to overestimate the usual situation. However, in spite of these qualifications the present calculations seem to raise some interesting issues concerning the near-field atmospheric perturbations caused by the auroral electrojet, such as the possibility of air turbulence generation in the auroral zone during severe geomagnetic storms.

REFERENCES

Beer, T., *Atmospheric Waves*, John Wiley, New York, 1974.
Blumen, W., and R. G. Hendl, On the role of Joule heating as a source of gravity wave energy above 100 km, *J. Atmos. Sci.*, *26*, 210, 1969.
Brekke, A., On the relative importance of Joule heating and the Lorentz force in generating atmospheric gravity waves and infrasound waves in the auroral electrojets, *J. Atmos. Terr. Phys.*, *41*, 475, 1979.
Brekke, A., and C. L. Rino, High-resolution altitude profiles of the auroral zone energy dissipation due to ionospheric currents, *J. Geophys. Res.*, *83*, 2517, 1978.
Butkov, E., *Mathematical Physics*, Addison-Wesley, Reading, Mass., 1968.
Chimonas, G., Infrasonic waves generated by auroral currents, *Planet. Space Sci.*, *18*, 591, 1970.
Chimonas, G., and C. O. Hines, Atmospheric gravity waves launched by auroral currents, *Planet. Space Sci.*, *18*, 565, 1970.
Chimonas, G., and W. R. Peltier, The bow wave generated by an auroral arc in supersonic motion, *Planet. Space Sci.*, *18*, 599, 1970.
Chiu, Y. T., Planetary scale wave response to auroral heating of the neutral atmosphere, *J. Geophys. Res.*, *81*, 1231, 1976.
Davis, M. J., On polar substorms as the source of large-scale traveling ionospheric disturbances, *J. Geophys. Res.*, *76*, 4525, 1971.
Francis, S. H., A theory of medium-scale traveling ionospheric disturbances, *J. Geophys. Res.*, *79*, 5245, 1974.
Friedman, J. P., Propagation of internal gravity waves in a thermally stratified atmosphere, *J. Geophys. Res.*, *71*, 1033, 1966.
Greenwald, R. A., W. L. Ecklund, and B. B. Balsley, Auroral currents, irregularities, and luminosity, *J. Geophys. Res.*, *78*, 8193, 1973.
Greenwald, R. A., W. L. Ecklund, and B. B. Balsley, Radar observations of auroral electrojet currents, *J. Geophys. Res.*, *80*, 3635, 1975.
Hines, C. O., and C. A. Reddy, On the propagation of atmospheric gravity waves through regions of wind shear, *J. Geophys. Res.*, *72*, 1015, 1967.
Hunsucker, R. D., Estimate of the relative importance of Joule heat-

ing and the Lorentz force in generating atmospheric gravity waves from the auroral electrojet, *J. Geophys. Res., 82,* 4826, 1977.

Richmond, A. D., and S. Matsushita, Thermospheric response to a magnetic substorm, *J. Geophys. Res., 80,* 2839, 1975.

Testud, J., Gravity waves generated during magnetic substorms, *J. Atmos. Terr. Phys., 32,* 1793, 1970.

Waco, D. E., A statistical analysis of wind and temperature variables associated with high altitude clear air turbulence (HICAT), *J. Appl. Meteorol., 9,* 300, 1970.

Wilson, C. R., Infrasonic wave generation by aurora, *J. Atmos. Terr. Phys., 37,* 973, 1975.

Woods, J. D., On Richardson's number as a criterion for laminar-turbulent-laminar transition in the ocean and atmosphere, *Radio Sci., 4,* 1289, 1969.